ELSEVIER

International Journal of Heat and Fluid Flow 22 (2001) 657–665

International Journal of HEAT AND FLUID FLOW

www.elsevier.com/locate/ijhff

Thermodynamic optimization of finned crossflow heat exchangers for aircraft environmental control systems

Jose V.C. Vargas, Adrian Bejan *

Department of Mechanical Engineering and Materials Science, School of Engineering, Duke University, Box 90300, Durham, NC 27708-0300, USA

Received 5 April 2001; accepted 10 June 2001

Abstract

This paper shows that the main geometric features of a flow component can be deduced from the thermodynamic optimization of the global performance of the largest flow system that incorporates the component. This approach represents a departure from the usual approach, where a flow component is optimized in isolation. The example chosen is the counterflow heat exchanger of the environmental control system (ECS) used on modern aircraft. The heat exchanger is fitted with a diffuser and a nozzle for the ram air, and the ECS runs on the boot strap air cycle, employing an additional compressor and turbine. Two heat transfer surface types are considered, finned and smooth parallel plates. Numerical results are reported for the external geometric aspect ratios of the heat exchanger, and for the plate-to-plate spacing of the smooth-plates model. It is shown that the optimized geometry for the core with finned surfaces is nearly the same as the optimized geometry for the core with smooth plates. Several of the optimized geometric features are robust with respect to changes in external parameters that vary from one application to the next. The method illustrated in this paper – the thermodynamic (constructal) optimization of flow geometry – is applicable to any system that runs on the basis of a limited amount of fuel (exergy) installed onboard, e.g., automobiles, ships, portable tools.

Keywords: Entropy generation minimization; Optimal geometry; Constructal design; Geometry; Topology; Thermodynamic optimization; Crossflow heat exchangers; Finned surfaces

1. Introduction

There are many modern engineering systems that function while being driven by the finite amount of fuel that is initially installed on board. They function 'better' when they perform the required tasks using less fuel. One important class of such applications is aircraft design. In this industry the need to accomplish more with less fuel is growing. Designers are complementing traditional optimization methods (e.g., the minimization of take-off gross weight) with methods based on the minimization of the destruction of fuel exergy in all the flow systems onboard. In principle, at least, thermodynamic optimization can deliver physical configuration (geometry, architecture, morphology) of all the flow systems and their components (Bejan, 2000).

In this paper we illustrate this geometric optimization process by focusing on one component (heat exchanger) of one flow system (environmental control system, or ECS) of a contemporary aircraft (Fig. 1). We have several reasons for making this choice. In the past, heat exchangers have been optimized thermodynamically by themselves, i.e., in isolation (e.g., Bejan, 1997; London and Shah, 1983; Sekulic and Herman, 1986; Sekulic, 1986; Poulikakos and Johnson, 1989; Krane, 1987; Witte and Shamsundar, 1983; Witte, 1988; Paoletti et al., 1989; Benedetti and Sciubba, 1993). The literature shows that the use of thermodynamic isolation requires special care on how the isolated system is defined. In this paper we move away from thermodynamic isolation, and optimize the global performance of the largest assembly: the entire environmental control system. We seek better global performance by varying all the free geometric features of one component: the heat exchanger core.

The thermodynamic imperfection of the heat exchanger is due to heat transfer and fluid flow processes, which are the main topics covered by this journal. The work that we describe documents the thermodynamics of such processes, i.e., the performance implications of the irreversibilities due to heat transfer and fluid flow.

Another reason for undertaking this study is the call for simplicity in modeling, analysis and numerical simulation and computation. Heat exchanger models are simpler and easier to implement when complications such as fins are neglected. This is why most of the existing work on the thermodynamic optimization is based on models using smooth parallel plates and smooth tubes. The objective of our work is to determine how

* Corresponding author. Tel.: +1-919-660-5309; fax: +1-919-660-8963.

E-mail address: dalford@duke.com (A. Bejan).

0142-727X/01/$ - see front matter
PII: S0142-727X(01)00129-1

Notation

A	heat transfer area, m^2
A_{cd}	diffuser inlet cross-sectional area, m^2; $\tilde{A}_{cd} = A_{cd}/(1\ m^2)$
$B_{a,e}$	channel spacings, m
b	constant, R/c_p
c_p	specific heat at constant pressure, J/kg K
D_h	hydraulic diameter, m
DHN	diffuser-heat exchanger-nozzle assembly
ECS	environmental control system assembly
f	friction factor
h	heat transfer coefficient, W/m^2 K
H	height, m
k	thermal conductivity, W/m K
$K_{c,e}$	loss coefficients for contraction and enlargement
$L_{x,y,z}$	lengths, m
$\dot{m}$	mass flow rate, kg/s
M	mass, kg
M	Mach number
n	number of elemental units
N	number of heat transfer units
N_S	entropy generation number
P	pressure, Pa
$\tilde{P}$	dimensionless pressure
Pr	Prandtl number
R	ideal gas constant, J/kg K
Re	Reynolds number
$\dot{S}_{gen}$	entropy generation rate, W/K
t	thickness, m
T	temperature, K
U	overall heat transfer coefficient, W/m^2 K
v	specific volume, m^3/kg
V	velocity, m/s
$\tilde{V}$	dimensionless velocity
V_t	total volume, m^3
w	dimensionless power
$\dot{W}$	power, W

Greek symbols

$\beta_{a,e}$	ratio (heat transfer area)/(volume between plates)
γ	ratio of specific heats, c_p/c_v
$\delta_{a,e}$	fin thickness, m
ΔP	pressure drop, Pa
η	isentropic efficiency
η_0	fin efficiency
μ	ratio of capacity rates
ρ	density, kg/m^3
σ	contraction ratio
ϕ	solid volume fraction

Subscripts

a	ambient, ram air
c	compressor
d	diffuser
e	engine-air stream
i	a or e
min	minimum
n	nozzle
opt	optimum
out	outlet
rev	reversible
t	turbine
w	wall

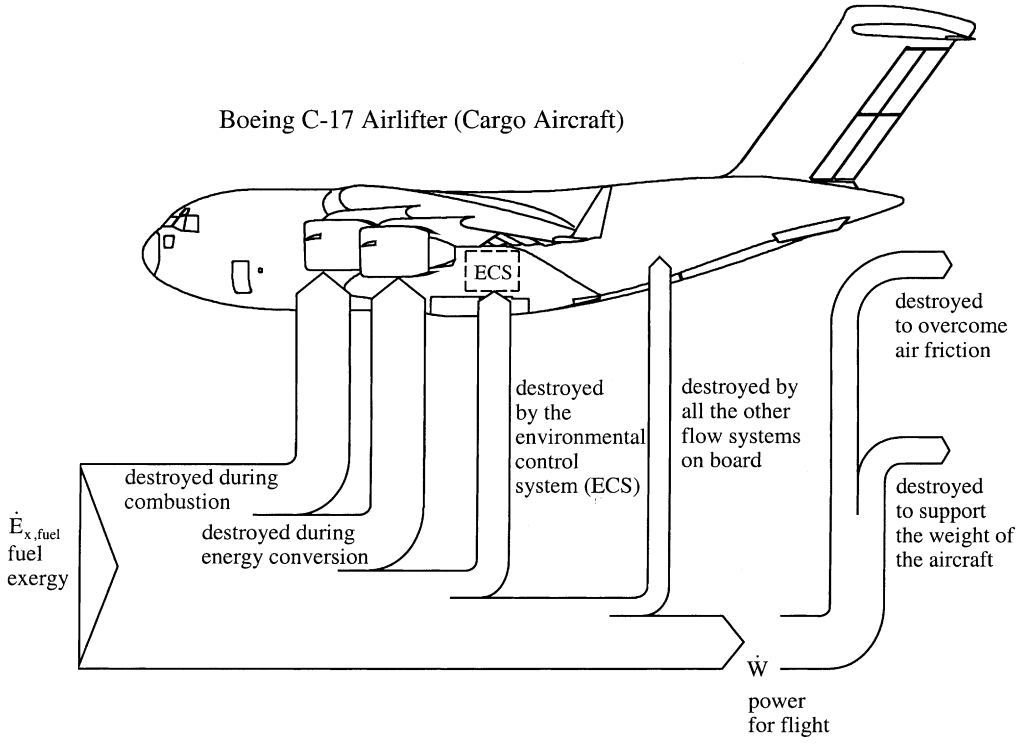

Fig. 1. The distribution of energy destruction on an aircraft.

important the 'finned' versus 'smooth' surface choice is. We do this by optimizing the geometry of the ECS heat exchanger both ways, in a model with finned surfaces of the type used currently in the aircraft industry, and in a model with smooth and parallel plates.

When should the global optimization of a flow system be based on entropy generation minimization? In brief, the methods of exergy analysis (EA), entropy generation minimization (EGM) and thermoeconomics (TE) are the most established changes that have taken place in modern engineering thermodynamics during the past three decades (e.g., Moran, 1982; Bejan, 1982; Feidt, 1996; Moran and Sciubba, 1994; Stecco and Moran, 1992; Krane, 1994, 1995; Bejan et al., 1996). The emphasis is now on identifying the mechanisms and system components that are responsible for thermodynamic losses (EA), the sizes of these losses (EA), minimizing the losses subject to the global constraints of the system (EGM), and minimizing the total costs associated with building and operating the energy system (TE). Thermodynamic optimization may be used by itself (without cost minimization) in the preliminary stages of design, in order to identify trends and the existence of optimization opportunities. The optima and structural characteristics identified based on thermodynamic optimization can be made more realistic through subsequent refinements based on global cost minimization.

Thermoeconomics, or cost minimization based on proper exergetic costing of features of thermodynamic imperfection, is the ultimate way to optimize the design (e.g., Lazzaretto and Tsatsaronis, 1997; Bejan et al., 1996). Thermodynamic optimization can be useful by itself, for orientation, in cases where the total cost of the installation is dominated by the cost due to thermodynamic irreversibility. The classical example of this kind is cryogenics, or refrigeration at very low temperatures, where the power requirement is substantial and proportional to the entropy generated in the cold space. Another example is the subject of this paper: environmental control systems for aircraft.

In Fig. 1 we show why thermodynamic optimization is an important consideration in aircraft flow-system design. Exergy is destroyed, or entropy is generated whenever streams and currents interact with each other and with components. On an aircraft there are many systems and processes that contribute to the ultimate destruction of all the exergy furnished by the fuel. Fig. 1 presents a summary of the distribution of losses, highlighting the losses that will be minimized as an ensemble in this study. Proceeding in the direction of fuel flow, the first exergy loss [about 30% (Dunbar and Lior, 1991)] is due to the combustion process. Next is the loss due to the irreversible operation of the engine. The remaining exergy fraction is the power produced by the engine, which drives all the subsystems and meets all the functions of the aircraft. Chief among functions is the power required to maintain the flight ($\dot{W}$), i.e. to overcome drag and to hold (support) the aircraft at its altitude. The power $\dot{W}$ is destroyed completely in the turbulent flow around the aircraft, especially in the wake.

The rest of the power generated by the engine is destroyed in the auxiliary systems, which are numerous. The dominant user of exergy is the environmental control system (ECS), which on a military transport plane such as the C-17 accounts for 64.6% of the engine power at cruise condition (Siems, 2001). The ECS itself is an assembly of subsystems, as shown in the example of Fig. 2. We show that the thermodynamic performance of the entire ECS can be maximized by selecting the geometric features of the crossflow heat exchanger. Next, we show that the optimized heat exchanger geometry can be determined by using a model with finned surfaces. We also show that certain features of the optimized geometry can be anticipated by using a heat exchanger model with smooth surfaces.

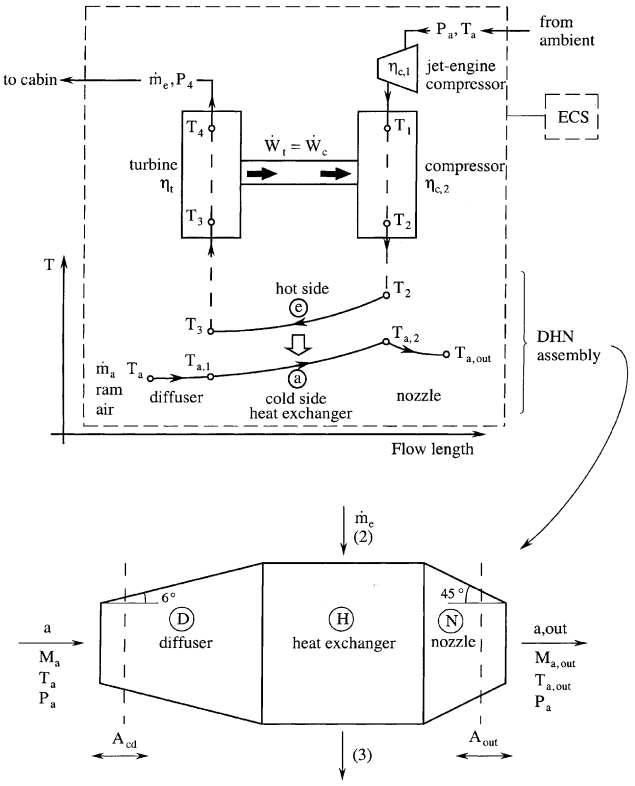

Fig. 2. ECS based on the bootstrap air cycle, and the assembly composed of the diffuser, heat exchanger and nozzle (DHN).

2. Environmental control system

The environmental control system (ECS) is represented schematically in Fig. 2. The thermodynamic cycle is known as the "boot strap air cycle". The upper stream $\dot{m}_e$ is originally drawn from the ambient (P_a, T_a), and is compressed to the state (P_1, T_1) in the low-pressure stages of the jet engine. This "engine-air" stream $(\dot{m}_e)$ is a fraction of the air flow rate processed by the jet-engine compressor. The stream $\dot{m}_e$ is compressed further in a separate compressor, which raises its pressure and temperature (P_2, T_2). Next, the stream temperature is lowered to T_3 in a crossflow heat exchanger, and then the stream is expanded through a turbine. The shaft power produced by the turbine is used to drive a separate compressor, $\dot{W}_t = \dot{W}_c$. The purpose of the expansion through the turbine is to decrease the pressure and temperature to the specified cabin conditions (P_4, T_4). The air flow rate $\dot{m}_e$ is specified by the environmental design requirements of the cabin.

The lower stream $\dot{m}_a$ shown in Fig. 2 is the "ram air" used on the cold side of the crossflow heat exchanger. The ram air enters the system at ambient conditions (P_a, T_a), and initially it has the same speed as the aircraft (V_a). It is decelerated to the state (a,1) in a diffuser, and continues through the heat exchanger, where it is heated to the state (a,2). Before being discharged into the ambient, the $\dot{m}_a$ stream is accelerated to the state (a,out). The ram air mass flow rate $\dot{m}_a$ is not specified.

The processes undergone by the engine-air and ram-air streams are irreversible. The compression process (1)–(2) is not

isentropic: the isentropic efficiency is $\eta_{c,2} < 1$. Similarly, the expansion (3)–(4) is characterized by the turbine isentropic efficiency $\eta_t < 1$. The flow (2)–(3) on the hot side of the heat exchanger is accompanied by the frictional pressure drop ΔP_e. The preliminary compression (a)–(1) is also irreversible: the isentropic efficiency of the engine compressor is $\eta_{c,1} < 1$.

The lower part of Fig. 2 shows the deceleration process (a)–(a,1) through the diffuser, where the isentropic efficiency is $\eta_d < 1$. The pressure drop experienced by the ram air while flowing on the cold side of the heat-exchanger surface is ΔP_a. The isentropic efficiency of the nozzle acceleration process (a,2)–(a,out) is $\eta_n < 1$.

3. Model

The analysis developed in this section establishes the relation between the entropy generation rate and the physical features of the system. To start with, the entropy generation rate due to the entire ECS system defined by the dashed line in Fig. 2 is

$$\dot{S}_{\mathrm{gen,ECS}} = \dot{m}_e\left[\left(c_p\ln\frac{T_1}{T_a} - R\ln\frac{P_1}{P_a}\right) + \left(c_p\ln\frac{T_2}{T_1} - R\ln\frac{P_2}{P_1}\right) + \left(c_p\ln\frac{T_3}{T_2} - R\ln\frac{P_3}{P_2}\right) + \left(c_p\ln\frac{T_4}{T_3} - R\ln\frac{P_4}{P_3}\right)\right]_e + \dot{m}_a\left(c_p\ln\frac{T_{out}}{T_{in}} - R\ln\frac{P_{out}}{P_{in}}\right)_a, \quad (1)$$

where ECS stands for environmental control system. The terms collected in this expression correspond to the sequence of components recognized in Fig. 2. The heat exchanger core is not analyzed in isolation. Its irreversibility is added to that of the entire ECS, and it is the ECS-assembly irreversibility that is minimized by varying the geometry of the core. The two fluids are modeled as ideal gases with constant specific heat, $(R, c_p)_e$ and $(R, c_p)_a$. It is convenient to introduce the non-dimensional variables:

$$\tilde{P} = \frac{P}{P_4}, \quad \tau = \frac{T}{T_4}, \quad (2)$$

$$N_S = \frac{\dot{S}_{\mathrm{gen,ECS}}}{\dot{m}_e c_{pe}}, \quad \mu = \frac{\dot{m}_a c_{pa}}{\dot{m}_e c_{pe}}, \quad (3)$$

where $(P_4, T_4, \dot{m}_e)$ are the fixed cabin conditions, N_S is the entropy generation number, and μ is the ratio of the two capacity rates. Eq. (1) becomes

$$N_S = \left(\ln\frac{\tau_1}{\tau_a} - b\ln\frac{\tilde{P}_1}{\tilde{P}_a}\right) + \left(\ln\frac{\tau_2}{\tau_1} - b\ln\frac{\tilde{P}_2}{\tilde{P}_1}\right) + \left(\ln\frac{\tau_3}{\tau_2} - b\ln\frac{\tilde{P}_3}{\tilde{P}_2}\right) + \left(\ln\frac{1}{\tau_3} - b\ln\frac{1}{\tilde{P}_3}\right) + \mu\ln\frac{\tau_{a,out}}{\tau_a}, \quad (4)$$

where $b = R/c_p$. Since the fluid is air, the two streams have the same b ratio, namely $b = 0.286$, which corresponds to $\gamma = c_p/c_v = 1.4$. Eq. (4) was abbreviated based on the observation that $P_{out} = P_{in} = P_a$.

In the method of entropy generation minimization (e.g., Bejan, 1996) the entropy generation calculation is complemented by the analysis of the heat flow and fluid flow through each component. This analysis accounts for the physical parameters and size constraints of the component. For the first component of our system – the engine compressor (a)–(1) in Fig. 2 – these effects are embodied in the specified compressor efficiency:

$$\eta_{c,1} = \frac{T_{1,rev} - T_a}{T_1 - T_a}. \quad (5)$$

Noting that $T_{1,rev} = T_a(P_1/P_a)^b$, Eq. (5) becomes

$$\tau_1 = \tau_a + \frac{\tau_a}{\eta_{c,1}}\left[\left(\frac{\tilde{P}_1}{\tilde{P}_a}\right)^b - 1\right]. \quad (6)$$

For the separate compressor (1)–(2) in Fig. 2, the definition of the isentropy efficiency $\eta_{c,2}$ and the first-law analysis yield

$$\tau_2 = \tau_1 + \frac{\tau_{1,a}}{\eta_{c,2}}\left[\left(\frac{\tilde{P}_2}{\tilde{P}_1}\right)^b - 1\right], \quad (7)$$

$$w_c = \frac{\tau_1}{\eta_{c,2}}\left[\left(\frac{\tilde{P}_2}{\tilde{P}_1}\right)^b - 1\right]. \quad (8)$$

In Eq. (8) the compressor power input w_c is dimensionless, $w_c = \dot{W}_c/(\dot{m}_e c_{pe} T_4)$.

The heat transfer between the two streams in the crossflow heat exchanger is described by the effectiveness-NTU relation (Incropera and DeWitt, 1990):

$$\varepsilon = 1 - \exp\left\{\mu N^{0.22}\left[\exp\left(-\mu^{-1}N^{0.78}\right) - 1\right]\right\}, \quad (9)$$

which is based on the assumption that $\dot{m}_e c_{pe}$ is the smaller of the two capacity rates (i.e., $\mu > 1$), and where N is the number of heat transfer units, $N = UA/(\dot{m}_e c_{pe})$. The definition of the effectiveness ε produces two relations between the inlet and outlet temperatures of the two streams,

$$\tau_2 - \tau_3 = \varepsilon(\tau_2 - \tau_{a,1}), \quad (10)$$

$$\tau_{a,2} - \tau_{a,1} = \frac{\varepsilon}{\mu}(\tau_2 - \tau_{a,1}). \quad (11)$$

Eqs. (9) and (11) hold for $\mu > 1$; the corresponding equations for $\mu > 1$ are not listed. The pressure drop along the hot side of the heat transfer surface, $\Delta\tilde{P}_e = \tilde{P}_2 - \tilde{P}_3$, is analyzed later in this section.

Downstream of the crossflow heat exchanger is the turbine (3)–(4) in Fig. 2: the definition of the efficiency η_t, and the first-law analysis of the turbine yield

$$\tau_3 = 1 + \eta_t\tau_3\left(1 - \tilde{P}_3^{-b}\right), \quad (12)$$

$$w_t = \eta_t\tau_3\left(1 - \tilde{P}_3^{-b}\right). \quad (13)$$

The dimensionless turbine power output is defined as $w_t = \dot{W}_t/(\dot{m}_e c_{pe} T_4)$. Finally, since the turbine drives the separate compressor, $w_t = w_c$ (a special case in fact), the first-law analysis of the turbine and compressor, combined, requires

$$\tau_2 - \tau_1 = \tau_3 - 1. \quad (14)$$

On the cold side of the system, we analyze the course followed by the ram air. This begins with the diffuser (a)–(a,1), for which the η_d definition and the first law of thermodynamics require

$$\eta_d = \frac{T_{a,1rev} - T_a}{T_{a,1} - T_a}, \quad (15)$$

$$c_{pa}(T_{a,1} - T_a) = \frac{1}{2}\left(V_a^2 - V_{a,1}^2\right), \quad (16)$$

where $T_{a,1rev} = T_a(P_{a,1}/P_a)^b$. The dimensionless equations (15) and (16) become

$$\frac{\tau_{a,1}}{\tau_a} - 1 = \frac{1}{\eta_d}\left[\left(\frac{\tilde{P}_{a,1}}{\tilde{P}_a}\right)^b - 1\right], \quad (17)$$

$$\frac{\tau_{a,1}}{\tau_a} - 1 = \frac{1}{2}\left(\tilde{V}_a^2 - \tilde{V}_{a,1}^2\right). \tag{18}$$

The dimensionless bulk velocity $\tilde{V} = V(c_{pa}T_a)^{1/2}$ is proportional to the Mach number $\mathrm{M} = V/(\gamma_a R_a T_a)^{1/2}$, or $\tilde{V} = \mathrm{M}(\gamma_a - 1)^{1/2}$. Invoking the conservation of the mass flow rate $\dot{m}_a$ in every cross-section A_c and the ideal gas model, namely $\dot{m}_a = \rho V A_c$ and $\rho = P/(RT)$, we write the Mach number as

$$\mathrm{M} = \frac{\dot{m}_a}{PA_c}\left(\frac{R_a}{\gamma_a}T\right)^{1/2}. \tag{19}$$

In sum, when the geometry and operating conditions are specified, Eqs. (17)–(19) pinpoint state (a,1), or $\tilde{P}_{a,1}$ and $\tau_{a,1}$.

The heating process (a,1)–(a,2) experienced by the $\dot{m}_a$ stream is governed by the effectiveness-NTU relations (9)–(11). The pressure drop $\Delta\tilde{P}_a = \tilde{P}_{a,1} - \tilde{P}_{a,2}$ is given by Eq. (24) later in this section.

Finally, the irreversible flow through the nozzle is described by the efficiency and first-law relations

$$\eta_n = \frac{T_{a,2} - T_{a,out}}{T_{a,2} - T_{a,out\,rev}}, \tag{20}$$

$$c_{pa}(T_{a,2} - T_{a,out}) = \frac{1}{2}\left(V_{a,out}^2 - V_{a,2}^2\right). \tag{21}$$

Recognizing that $T_{a,out\,rev} = T_{a,2}(P_a/P_{a,2})^b$ and using the non-dimensional variables employed earlier, we can non-dimensionalize equations (20) and (21) as

$$1 - \frac{\tau_{a,out}}{\tau_{a,2}} = \eta_n\left[1 - \left(\frac{\tilde{P}_a}{\tilde{P}_{a,2}}\right)^b\right], \tag{22}$$

$$\frac{\tau_{a,2}}{\tau_a} - \frac{\tau_{a,out}}{\tau_a} = \frac{1}{2}\left(\tilde{V}_{a,out}^2 - \tilde{V}_{a,2}^2\right). \tag{23}$$

For the pressure drops along the counterflow, $(\Delta P_e, \Delta P_a)$ we use the classical formulation (Kays and London, 1984):

$$\Delta P_i = \frac{1}{2}G_i^2 v_{i,in}\left[\left(K_{c,i} + 1 - \sigma_i^2\right) + 2\left(\frac{v_{i,out}}{v_{i,in}} - 1\right) + f_i\frac{A_i}{A_{c,i}}\frac{\overline{v_i}}{v_{i,in}} - \left(1 - \sigma_i^2 - K_{e,i}\right)\frac{v_{i,out}}{v_{i,in}}\right] \quad (i = e, a), \tag{24}$$

where

$$\overline{v_i} = \frac{1}{2}(v_{i,in} + v_{i,out}), \quad \sigma_{in} = \frac{A_{c,i}}{A_{f,i}}. \tag{25}$$

In these relations $G_i, v_i, A_i, f_i, \sigma_i, K_{c,i}, K_{e,i}, A_{c,i}$ and $A_{f,i}$ represent in order, the mass velocity $(G_i = \dot{m}_i/A_{c,i})$, the specific volume $(v_i = R_i T_i/P_i)$, the total heat transfer area, the friction factor, the cross-section contraction ratio, the contraction loss coefficient, the enlargement loss coefficient, the flow cross-section and the stream cross-section before entering the duct. The friction factor is available as a function of the Reynolds number based on hydraulic diameter, $f_i = f_i(Re_i)$, either as empirical correlations for parallel-plate channels, or as tabulated data for finned surfaces (Kays and London, 1984).

The same heat exchanger sources provide the heat transfer coefficient information needed for evaluating the number of heat transfer units N. The flow of heat across the A_i surface overcomes three thermal resistances in series,

$$\frac{1}{N} = \frac{\dot{m}_e c_{pe}}{UA} = \dot{m}_e c_{pe}\left(\frac{1}{\eta_{0,e}h_e A_e} + \frac{t_w}{k_w A_w} + \frac{1}{\eta_{0,a}h_a A_a}\right). \tag{26}$$

In this expression $\eta_{0,i}, t_w, k_a$ and A_w are the fin efficiencies of the finned surfaces, the thickness of the wall penetrated by heat transfer, the wall thermal conductivity, and the average heat transfer surface, $A_w = (A_e + A_a)/2$. The heat transfer coefficients (h_e, h_a) are available in dimensionless form, as the respective Stanton number versus the channel Reynolds number, $h_i(c_{pi}G_i) = St_i(Re_i)$, as tabulated data for finned surfaces (Kays and London, 1984) and as empirical correlations for the respective Nusselt number as a function of the friction factor and channel Reynolds number, $h_i D_{h,i}/k_i = Nu_i(f_i, Re_i)$.

4. Types of surfaces and constraints

The preceding analysis completes the model, and allows us to relate N_S to the irreversibilities and physical sizes of all the components. The numerical minimization of the entropy generation rate can proceed, but first we must specify the type of the heat transfer surface built into the crossflow heat exchanger. This assumption is necessary in order to access the f_i and St_i information that is available in the heat exchanger literature.

In this optimization study we assumed two different types of surfaces: (i) a typical assembly of finned surfaces that is used in the aircraft industry and (ii) smooth parallel plates with spacings B_e and B_a. Fig. 3 shows the main geometric features of the core of the crossflow heat exchanger. The selected

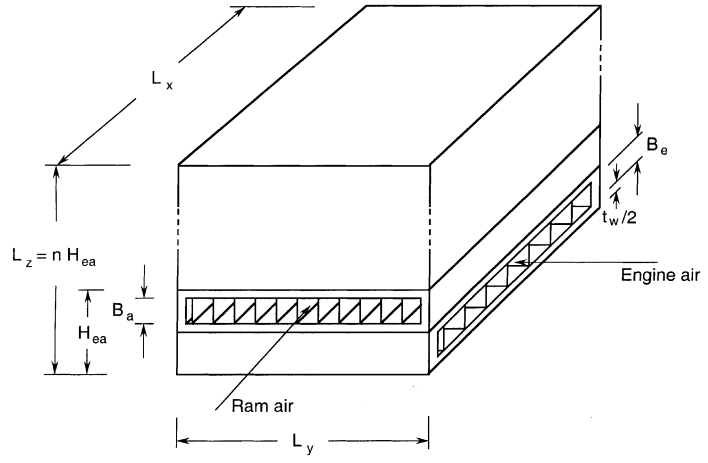

Fig. 3. The geometric features of the core of the crossflow heat exchanger.

typical aircraft configuration is (Kays and London, 1984; Siems, 2001):

(a) hot side: surface $20.06R(S) - 0.075/0.075 - 0.10(0) - 0.004$,

(b) cold side: surface $16.00R(S) - 0.125/0.125 - 0.125(0) - 0.0035$.

This encoded description follows the standards established in the finned surfaces heat exchangers literature (Dieckmann et al., 1972; Kays and London, 1984). From that description, the necessary f_i and St_i information is obtained from the data tabulated in Kays and London (1984). As shown schematically in Fig. 3, both surfaces have rectangular fin cross-section in the flow direction, with a single fin sandwich construction, i.e., no separation plate in the section.

In the parallel-plates configuration, empirical correlations were used to obtain the necessary friction factor and heat transfer coefficient data for the mathematical model. For the laminar regime ($Re_{D_h} < 2300$) we used the friction factor and heat transfer coefficient correlations (e.g., Bejan, 1993),

$$f_i = \frac{24}{Re_{D_{h,i}}} \quad \frac{h_i D_{h,i}}{k_i} = 8.235, \tag{27}$$

where $D_{h,i} = 2B_i$, $Re_{D_{h,i}} = G_i D_{h,i}/\mu_i$ and i = e,a. The correlations used for the turbulent regime were (e.g., Bejan, 1993)

$$f_i = 0.079 Re_{D_{h,i}}^{-1/4} \quad \left(2300 < Re_{D_{h,i}} < 2 \times 10^4\right), \tag{28}$$

$$\frac{h_i D_{h,i}}{k_i} = \frac{(f_i/2)\left(Re_{D_{h,i}} - 10^3\right)Pr_i}{1 + 12.7(f_i/2)^{1/2}\left(Pr_i^{2/3} - 1\right)} \quad \left(2300 < Re_{D_{h,i}} < 5 \times 10^6\right). \tag{29}$$

The height H_{ea} of the elemental channel unit is defined as the height of the assembly composed of one engine-air passage and one ram-air passage,

$$H_{ea} = B_e + B_a + 2t_w. \tag{30}$$

If n is the number of elemental units in the stack, the height of the heat exchanger core is

$$L_z = nH_{ea}. \tag{31}$$

The total volume of the core is constrained, $V_t = L_x L_y L_z$ = constant or, non-dimensionally, as $\tilde{V}_t = V_t/(1\ \mathrm{m}^3)$ = constant. This constraint is justified, because space is very valuable in most vehicle applications, particularly in aircraft design. The length scale $V_t^{1/3}$ is used for the purpose of non-dimensionalizing all the lengths that define this geometry,

$$\left(\tilde{B}_e, \tilde{B}_a, \tilde{t}_w, \tilde{H}_{ea}, \tilde{L}_x, \tilde{L}_y, \tilde{L}_a\right) = \left(B_e, B_a, t_w, H_{ea}, L_x, L_y, L_z\right)/V_t^{1/3} \tag{32}$$

such that the non-dimensionalized volume constraint reads

$$\tilde{L}_x \tilde{L}_y \tilde{L}_z = 1. \tag{33}$$

In the optimization of the parallel-plates configuration, there is another constraint: the total volume (or weight) of the wall material, $2nL_xL_yt_w$. The weight constraint is also justified. According to constructal theory, the minimal work required for flight is proportional to the body weight (Bejan, 2000, p. 239). The weight constraint is best represented by the volume fraction ϕ ($\ll 1$) occupied by the wall material in the entire volume, $\phi = 2nL_xL_yt_w/V_t$, constant, or

$$\phi = 2n\frac{\tilde{t}_w}{\tilde{L}_z} = 2n\tilde{L}_x\tilde{L}_y\tilde{t}_w \quad \text{(constant)}. \tag{34}$$

The diffuser is characterized by its inlet cross-sectional area, A_{cd}, or, non-dimensionally, $\tilde{A}_{cd} = A_{cd}/(1\ \mathrm{m}^2)$, which is taken as a specified external parameter in the design.

According to Fig. 3 the architecture of the heat exchanger core is determined completely if we specify six dimensions: L_x, L_y, L_z, B_e, B_a and t_w. For the parallel-plates configuration, there are two constraints, Eqs. (33) and (34) and the reasonable assumption that the wall thickness is a specified parameter ($\tilde{t}_w \ll 1$) dictated by the availability of standard sizes of sheet metal. In conclusion, the geometric design of the core with smooth parallel plates has three degrees of freedom.

In the typical configuration used for aircraft ECS applications, once the finned surfaces are selected, several features are also fixed: the plate spacings B_i, the hydraulic diameters D_{hi}, the fin thicknesses δ_i, the ratios (transfer area)/(volume between plates) β_i, and the fin efficiencies $\eta_{0,i}$. Consequently, the solid volume fraction is also fixed, and is calculated as follows:

$$\phi = \frac{(\beta B\delta)_e + (\beta B\delta)_a + 2t_w}{H_{ea}}. \tag{35}$$

The characteristics of the selected surfaces (a, b) are such that $\phi = 0.268$ and $B_e/B_a = 0.789$. Because ϕ, B_e and B_a are fixed, we need to select only L_x, L_y and L_z, subject to the total volume constraint, Eq. (33). In conclusion, the geometric design of the finned core has only two degrees of freedom. According to the usual approach followed in the aircraft industry, when the core fin geometry and design performance conditions are known, the core volume is determined by an iterative approach. The unknowns are the core dimensions: L_x, L_y and L_z (Dieckmann et al., 1972).

5. Results for finned surfaces

The model described in Sections 3 and 4 allows the computation of the entropy generation number, N_S, which is defined by Eq. (4). For this calculation we must assume a set of representative physical values (Table 1), a set of external parameters (M, A_{cd}, ϕ and $\tilde{P}_1$) and values for the geometric variables ($L_y/L_x, L_z/L_x$ and B_e/B_a). In the case of finned surfaces, only L_y/L_x and L_z/L_x can be varied. Eqs. (5)–(34) are then combined to form a non-linear system of 11 non-dimensional equations and 11 unknowns ($\tau_{a,1}$, $\tilde{P}_{a,1}$, $\tau_{a,2}$, $\tilde{P}_{a,2}$, τ_2, $\tilde{P}_2$, τ_3, $\tilde{P}_3$, ε, $\tilde{A}_{c,out}$ and $\tau_{a,out}$). This system was solved by functional iteration. A maximum tolerance of 10^{-6} was imposed on $\|R\|$, which is the residual norm of the resulting system of non-linear equations. The numerical optimization was performed by varying $L_y/L_x, L_z/L_x$ and B_e/B_a for the core with smooth plates, and L_y/L_x and L_z/L_x for the core with finned surfaces. The external parameters M, $\tilde{A}_{cd}$, $\tilde{V}_t$ and $\tilde{P}_1$ were the same in both cases. The objective was to identify the optimal set of geometric parameters such that N_S is minimal.

We found numerically that N_S has minima with respect to each of the geometric degrees of freedom. The minimization of N_S is performed in a sequence of nested loops. The set of geometric parameters was varied in such a way that only in-

Table 1
Physical values used as reference case in the numerical optimization of the overall system

$c_p = 1$ kJ/kg K	$T_4 = 283.2$ K
$k_w = 20.8$ W/m K	$V_t = 1\ \mathrm{m}^3$
$\dot{m}_e = 0.7$ kg/s	$\gamma = 1.4$
$P_a = 0.03$ MPa	$\eta_{c,1} = 0.9$
$P_4 = 0.1$ MPa	$\eta_{c,2} = 0.7$
$Pr = 0.72$	$\eta_d = 0.97$
$R = 287$ J/kg K	$\eta_n = 0.95$
$t_w = 0.6$ mm	$\eta_t = 0.8$
$T_a = 244.5$ K	

teger values of elemental channels, n, were considered, such that the volume constraint was respected.

The first part of the results shows the optimization of the typical assembly of finned surfaces used in the aircraft industry. It is a two-way optimization process, namely, the optimization with respect to L_z/L_x and L_y/L_x. Fig. 4 illustrates the last step in the optimization process for a given set of external parameters, M, $\tilde{A}_{cd}$, $\tilde{V}_t$ and $\tilde{P}_1$. The $N_{S,m}$ values plotted on the ordinate were obtained after minimizing N_S with respect to L_z/L_x. The subscript m indicates that $N_{S,m}$ was minimized once. In the range $25 \lesssim L_y/L_x \lesssim 50$, $N_{S,m}$ has a relatively flat minimum – the changes in $N_{S,m}$ are less than 5%. This feature suggests that the discretization of the $(L_y/L_x, L_z/L_x)$ domain does not have to be highly refined during the optimization process, and that the computational time needed to identify the optimal design can be reduced.

Fig. 5 is a summary of the results of minimizing the global N_S with respect to L_y/L_x and L_z/L_x. The two-way optimization that was performed is indicated by the mm subscript on N_S. The figure also reports the optimized L_y/L_x and L_z/L_x ratios, and the corresponding number of elemental units in the core. The abscissa parameter accounts for the effect of varying the compressor bleed pressure P_1. The minimized entropy generation rate $(N_{S,mm})$ and the optimized ratio L_y/L_x increase monotonically as $\tilde{P}_1$ increases. The optimized ratio L_z/L_x decreases with $\tilde{P}_1$, and later becomes insensitive to further increases in $\tilde{P}_1$.

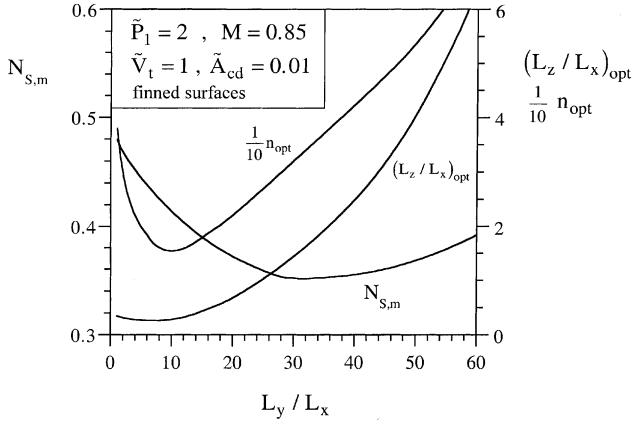

Fig. 4. The optimization of thermodynamic performance and geometry by varying L_y/L_x in the heat exchanger with finned surfaces.

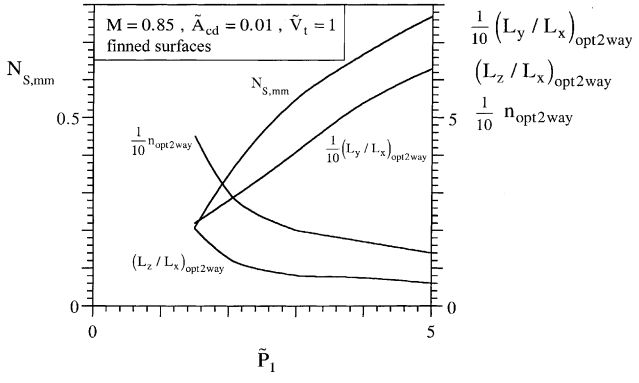

Fig. 5. The effect of the compressor bleed pressure on the optimized performance and geometry of the heat exchanger with finned surface.

The effect of the total core volume on the optimized finned core architecture is reported in Fig. 6. The geometric ratios L_y/L_x and L_z/L_x increase weakly as $\tilde{V}_t$ increases, indicating a certain degree of robustness in optimized architecture. Robustness is also indicated by the optimized L_y/L_x ratio plotted in Fig. 7, which shows the effect of varying the diffuser cross-section $\tilde{A}_{cd}$. In Fig. 8 we see that the effect of Mach number is relatively weak on $N_{S,mm}$, while both L_y/L_x and L_z/L_x decrease sharply as M increases. Taken together, Figs. 5–8 show how to

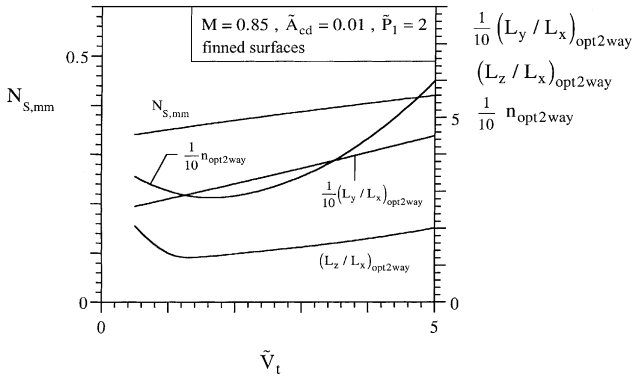

Fig. 6. The effect of the total core volume on the optimized performance and geometry of the heat exchanger with finned surfaces.

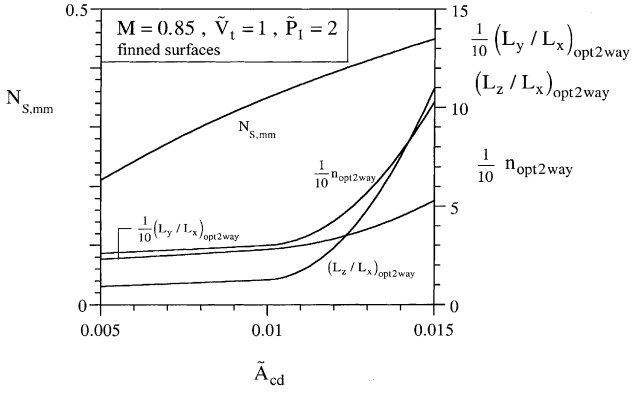

Fig. 7. The effect of the diffuser cross-section on the optimized performance and geometry of the heat exchanger with finned surfaces.

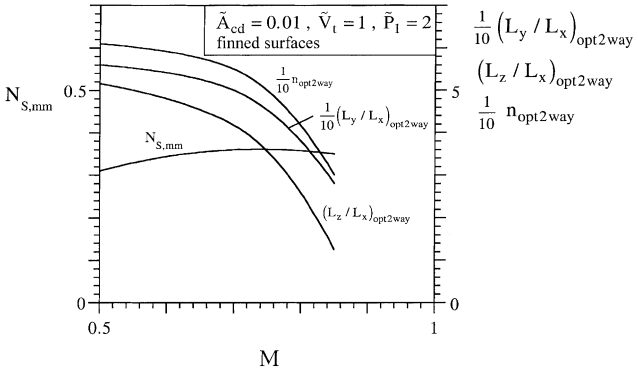

Fig. 8. The effect of the Mach number on the optimized performance and geometry of the heat exchanger with finned surfaces.

select the dimensions of the finned heat exchanger when the external parameters $(\tilde{P}_l, \tilde{V}_t, \tilde{A}_{cd}, M)$ are specified.

6. Results for smooth parallel plates

The next question is this: how important is it to conduct the optimization of a heat exchanger by working with the actual surface types that are preferred by industry? The assumption of certain surface types has the effect of constraining the design. On the contrary, the use of theoretical surfaces such as smooth parallel plates enlarges the design space (three degrees of freedom for smooth plates, instead of two for finned surfaces), and makes the modeling much easier because of classical and well-tested formulas such as Eqs. (27)–(29).

To answer this question we repeated the optimization of geometry by assuming smooth plates, and by fixing the solid volume fraction to the value of the finned case optimized in the preceding section ($\phi = 0.268$). We optimized the external aspect ratios of the core, L_y/L_x and L_z/L_x, and the internal ratio of channel spacings B_e/B_a. The result of minimizing N_S with respect to the three degrees of freedom is shown as the $N_{S,mmm}^{smooth}$ curve in Fig. 9. We reproduced on this graph the $N_{S,mm}$ curve of Fig. 5, which now is labeled $N_{S,mm}^{finned}$. The two N_S curves show the same order of magnitude, and the same trend with respect to the abscissa parameter $\tilde{P}_l$. The smooth-plates optimization underestimates the global entropy generation rate especially as $\tilde{P}_l$ increases.

Fig. 9 also shows one of the optimized geometric features (L_z/L_x), and how it depends on the assumption of finned surfaces versus smooth plates. Again, both assumptions lead to approximately the same optimized aspect ratio, and the same trend with respect to changes in $\tilde{P}_l$. The second optimized aspect ratio (L_y/L_x) is even less sensitive to the heat transfer surface model (Fig. 10), in fact, it is hard to distinguish between the two curves. The only major difference is the optimized ratio of spacings, B_e/B_a, which applies only to the smooth-plates model, and which is reported in the lower part of Fig. 10. This is the reason why there is an order of magnitude difference between the numbers of elemental units (n) of the finned and smooth configurations. There are more units in the optimized smooth-plates model: the plate-to-plate spacings are smaller because they correspond to the hydraulic radii of the finned spaces, not to the spacings between the separating walls of the channels with fins (Fig. 3).

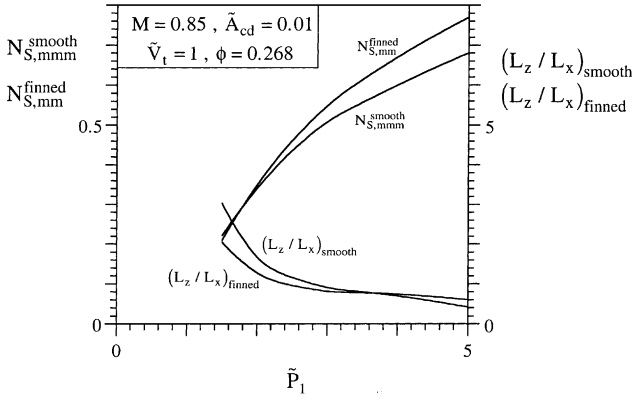

Fig. 9. The effect of the heat transfer surface model (finned versus smooth) on the optimized thermodynamic performance and the aspect ratio L_z/L_x.

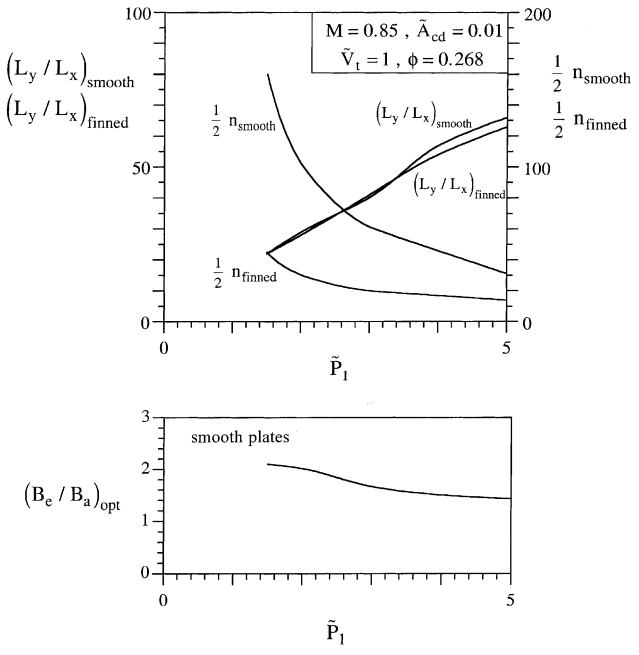

Fig. 10. The effect of the heat transfer surface model (finned versus smooth) on the aspect ratio L_y/L_x and the number of elemental units.

7. Concluding remarks

In summary, from the comparison shown in Figs. 9 and 10 we draw the important conclusion that the use of a simpler model (e.g., smooth surfaces) can anticipate geometric features that could ultimately be optimized based on a more realistic model (e.g., finned surfaces). Examples of such features are the external aspect ratios, L_y/L_x and L_z/L_x. The shortcoming of the method is that not all the geometric features of the optimized simple model are relevant to the selection of features and dimensions in the real applications. In Fig. 10, the number of elemental units n_{smooth} and the ratio of channel spacings are features inherited from the simple model, and they do not have immediately identifiable features in the more realistic model.

With such words of caution in mind, the use of smooth-surface models in the geometric optimization of heat exchanger structures is justified, especially as a preliminary step, to show the designer what can be expected when a more realistic surface model is implemented in the numerical optimization of flow architecture.

Another important aspect of the optimized geometrical features reported in this paper is the robustness, or the relative insensitivity of some of the results relative to significant changes in the regime of operation. The latter is represented by the external parameters that occupied the abscissas of Figs. 5–10. Noteworthy examples of relatively constant results of the optimization of geometry were the ratio L_z/L_x in Figs. 5 and 6, and the ratio L_y/L_x in Fig. 7. Robustness helps the engineered system in two ways. It allows an architecture optimized for one set of conditions to perform at near-maximum levels when forced to operate outside the narrow domain for which it was optimized. The other benefit is that relatively invariant geometric features need not be optimized to perfection. This simplifies the numerical optimization because it decreases the number of possible architectures the performances of which must be evaluated and compared.

The chief contribution of the work presented in this paper is that it focuses attention on the palpable result of the method of constructal optimization. That result is the morphology of the

flow system, which in a free design is unknown at the start of the optimization process. The flow system morphs into the best shapes and structures as the designer pursues the maximization of global performance subject to global constraints (Bejan, 2000). The performance and constraints are global because they refer to the entire system that uses the subsystem (or component) the architecture of which is optimized. In this paper, the environmental control system for an aircraft was used as an example from a vitally important technology. The method that we used is generally applicable to other systems that function based on the fuel exergy installed in finite amounts onboard, e.g., automobiles, ships, military vehicles and weapons systems, portable tools and environment-controlling suits.

Acknowledgements

The authors acknowledge with gratitude the guidance provided in this research project by Mr. David L. Siems of the Boeing Corporation. This material is based upon work supported by the Air Force Office of Scientific Research under Contract No. F49620-98-C-0007. Any opinions, findings and conclusions or recommendations are those of the authors and do not necessarily reflect the views of the Air Force Office of Scientific Research.

References

Bejan, A., 1982. Entropy Generation through Heat and Fluid Flow. Wiley, New York.

Bejan, A., 1993. Heat Transfer. Wiley, New York.

Bejan, A., 1996. Entropy Generation Minimization. CRC Press, Boca Raton, FL.

Bejan, A., 1997. Advanced Engineering Thermodynamics, 2nd ed. Wiley, New York.

Bejan, A., 2000. Shape and Structure from Engineering to Nature. Cambridge University Press, Cambridge, UK.

Bejan, A., Tsatsaronis, G., Moran, M., 1996. Thermal Design and Optimization. Wiley, New York.

Benedetti, P., Sciubba, E., 1993. Numerical calculation of the local rate of entropy generation in the flow around a heated finned tube. In: ASME HTD, 266, pp. 81–91.

Dieckmann, R.R., Watson, A.C., Glover, S.F., 1972. Development of integrated environmental control system designs for aircraft. Volume I-ECS Design, Technical Report AFFDL-TR-72-9 Air Force Flight Dynamics Laboratory Wright-Patterson Air Force Base, OH.

Feidt, M., 1996. Thermodynamique et Optimisation Energetique des Systemes et Procedes, 2nd ed. Technique et Documentation, Lavoisier Paris.

Incropera, F.P., DeWitt, D.P., 1990. Fundamentals of Heat and Mass Transfer, 3rd ed. Wiley, New York.

Kays, W.M., London, A.L., 1984. Compact Heat Exchangers, 3rd ed. McGraw-Hill, New York.

Krane, R.J., 1987. A second law analysis of the optimum design and operation of thermal energy storage systems. Int. J. Heat Mass Transfer 30, 43–57.

Krane, R.J., 1994. Thermodynamics and the Design, Analysis, and Improvement of Energy Systems 1994, AES-Vol. 33. ASME, New York.

Krane, R.J., 1995. Thermodynamics and the Design, Analysis, and Improvement of Energy Systems 1995, AES-Vol. 35. ASME, New York.

Lazzaretto, A., Tsatsaronis, G., 1997. On the quest for objective equations in exergy costing. In: Proceedings of the ASME Advanced Energy Systems Division, AES-Vol. 37, pp. 197–210.

London, A.L., Shah, R.K., 1983. Costs and irreversibilities in heat exchanger design. Heat Transfer Eng. 4, 59–73.

Moran, M.J., 1982. Availability Analysis: A Guide to Efficient Energy Use. Prentice-Hall, Englewood Cliffs, NJ.

Moran, M.J., Sciubba, E., 1994. Exergetic analysis: principles and practice. J. Eng. Gas Turbines Power 116, 285–290.

Paoletti, S., Rispoli, F., Sciubba, E., 1989. Calculation of exergetic losses in compact heat exchanger passages. In: ASME AES, 10-2, pp. 21–29.

Poulikakos, D., Johnson, J.M., 1989. Second law analysis of combined heat and mass transfer phenomena in external flow. Energy 14, 67–73.

Sekulic, D.P., 1986. Entropy generation in a heat exchanger. Heat Transfer Eng. 7, 83–88.

Sekulic, D.P., Herman, C.V., 1986. One approach to irreversibility minimization in compact crossflow heat exchanger design. Int. Comm. Heat Mass Transfer 13, 23–32.

Siems, D.L., 2001. Personal communication. The Boeing Company. St. Louis, MO.

Stecco, S.S., Moran, M.J., 1992. Energy for the Transition Age. Nova Science, New York.

Witte, L.C., 1988. The influence of availability costs on optimal heat exchanger design. J. Heat Transfer 110, 830–835.

Witte, L.D., Shamsundar, N.A., 1983. A thermodynamic efficiency concept for heat exchanger devices. J. Eng. Power 105, 199–203.